Electronic Supplementary Information

Architecting a nonlinear hybrid crystal-glass metamaterial fiber for all-optical photonic integration

Chien-Chih Lai,*[ab] Chia-Yao Lo,[c] Jian-Zhi Huang,[b] Chien-Chou Fang Chiang,[a] Duc Huy Nguyen,[a] Yu-Peng Chen[d] and Chun-Da Liao[e]

[a]*Department of Physics and* [b]*Department of Opto-Electronic Engineering, National Dong Hwa University, Hualien 97401, Taiwan*

[c]*Institute of Optoelectronic Sciences, National Taiwan Ocean University, Keelung 202, Taiwan*

[d]*Department of Applied Materials and Optoelectronic Engineering, National Chi Nan University, Nantou 54561, Taiwan*

[e]*School of Physics and Astronomy, Schuster Building, University of Manchester, Manchester M13 9PL, United Kingdom*

*Corresponding author:
E-mail: cclai@gms.ndhu.edu.tw
Department of Physics and Department of Opto-Electronic Engineering
National Dong Hwa University
Shoufeng, Hualien 97401, Taiwan

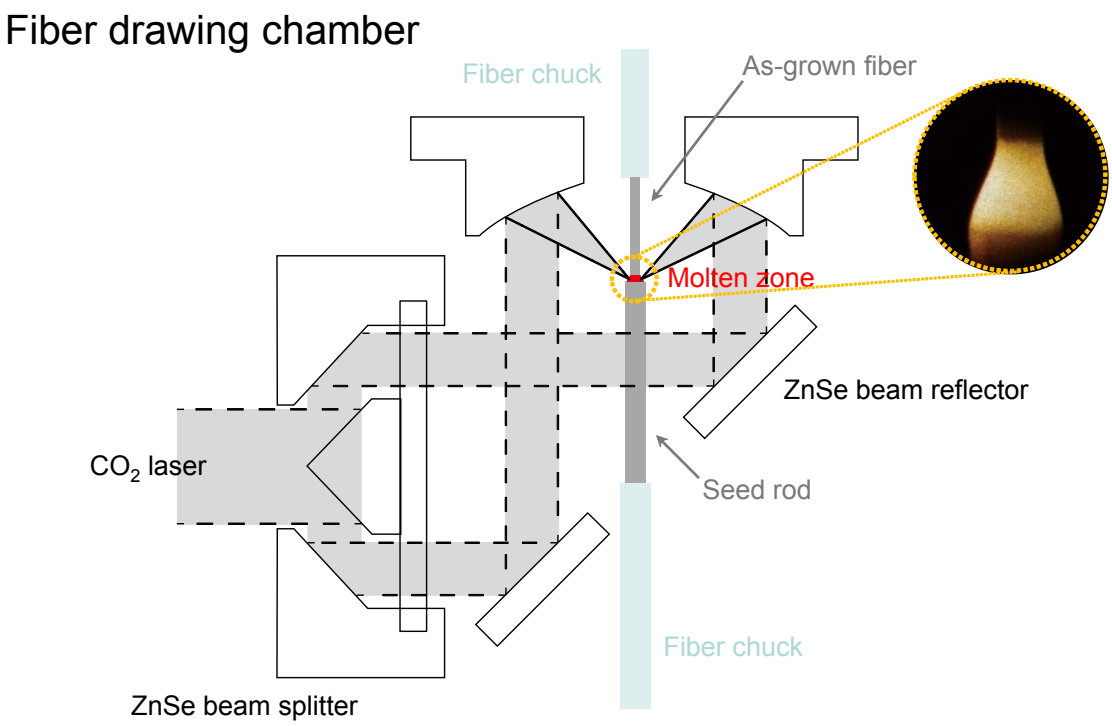

Figure S1. Schematics of the growth chamber of the laser-based fiber drawing system. A 10.6-μm CO_2 laser beam incidents into a ZnSe-based beam expander before entering the growth chamber. The beam diameter was expanded to 30 mm. All reflective mirrors were coated by gold on the copper substrates with high heat dissipation. The fiber chucks were driven by a stepping motor with a gearbox to reduce vibration. The motorized linear stage and laser power feedback were well-controlled by LabVIEW software. Inset: *In-situ* OM image of the molten zone showing the crateriform shape held by the surface tension.[1]

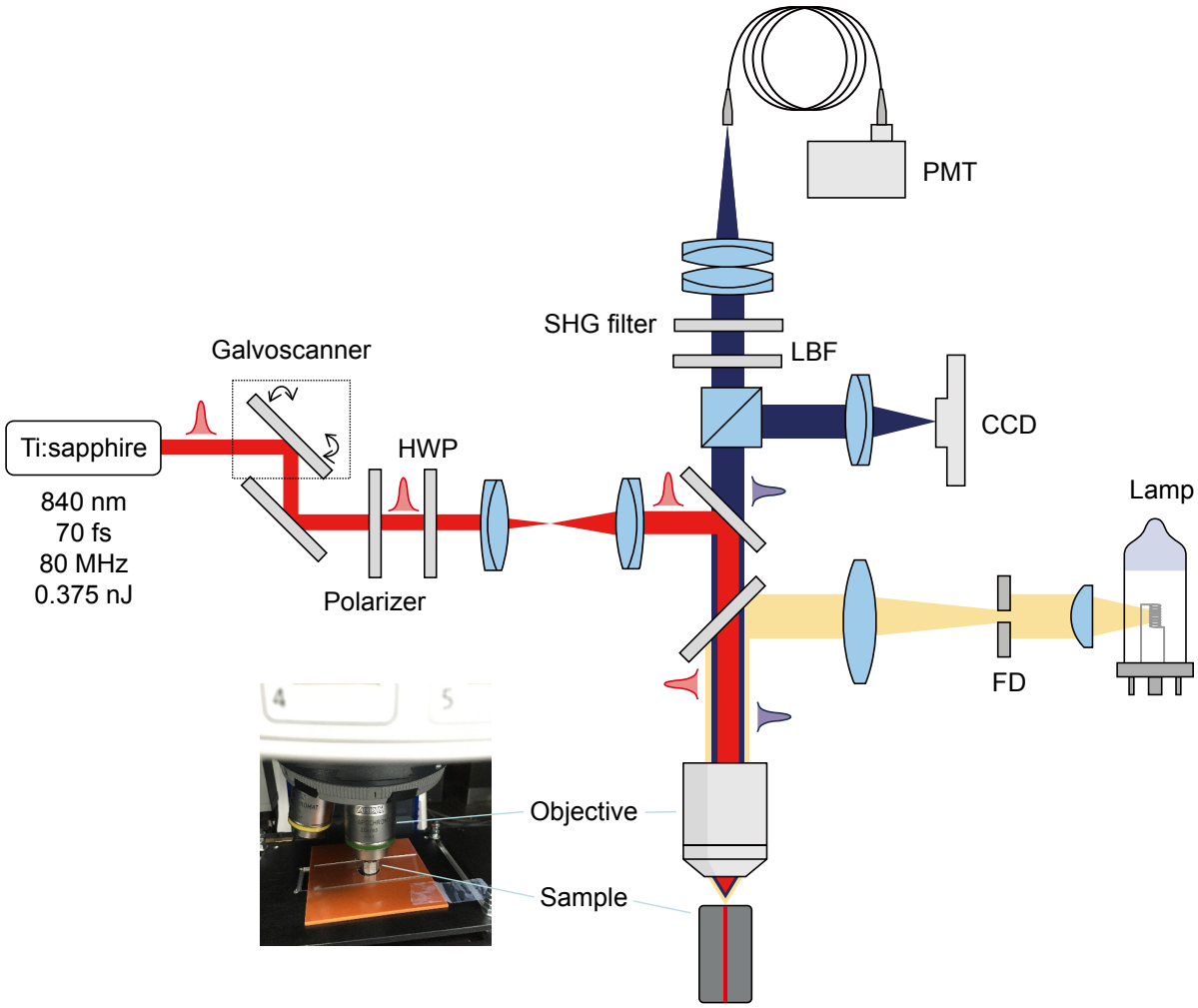

Figure S2. Schematics of the 2D SHG measurement. SHG characterizations were performed using a home-built laser-scanning confocal microscope, capable of conducting standard spectroscopic investigations.[2] 840-nm ultrafast femtosecond laser pulse generated from a Ti:sapphire laser, tunable between 680 and 1080 nm, was focused onto the end facet of the sample in an upright optical microscope (AXIO, Zeiss), as shown in the inset. All the SHG experiments in this study were conducted at a 10-kHz scanning rate in a 50 μm × 50 μm area. (HWP: half-wave plate; LBF: laser blocking filter; PMT: photomultiplier tube; CCD: charge coupled device; FD: field diaphragm)

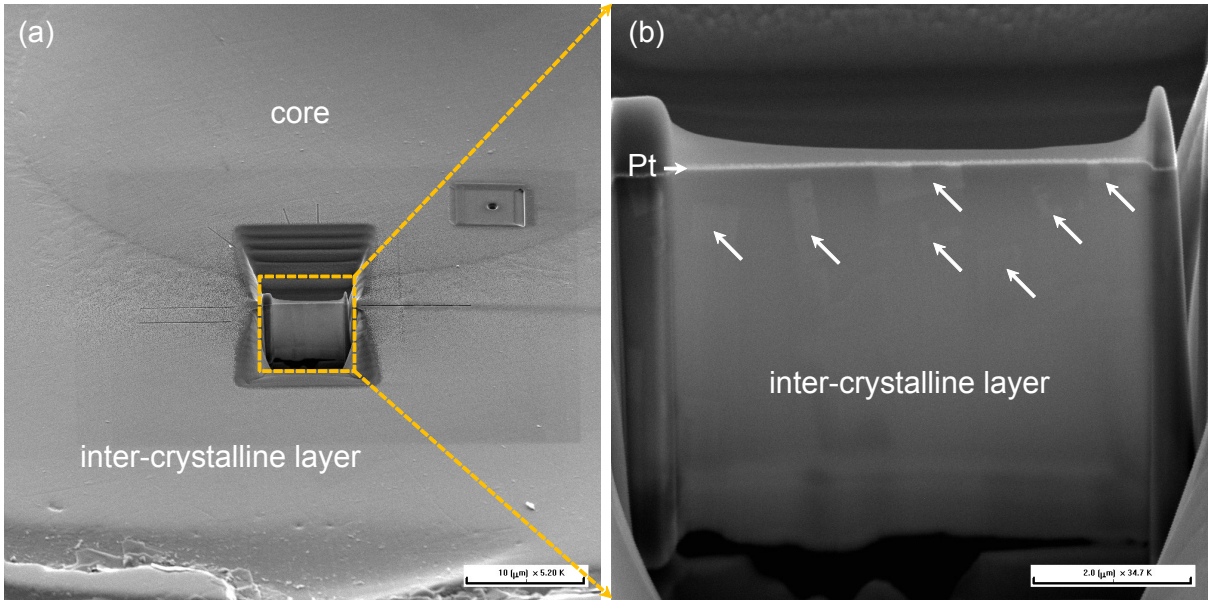

Figure S3. Preparation of HRTEM specimens by FIB nanomilling. (a) Low-magnification SEM image of a fiber specimen cut perpendicular to the growth direction of the dendrites in the inter-crystalline layer. (b) Close view of the dashed box in (a) showing a considerable amount of dispersed dendritic crystallites with *L*-shaped morphology, as marked by arrows. The top bright part is the deposited Pt layer; the bottom dark part is the sample.

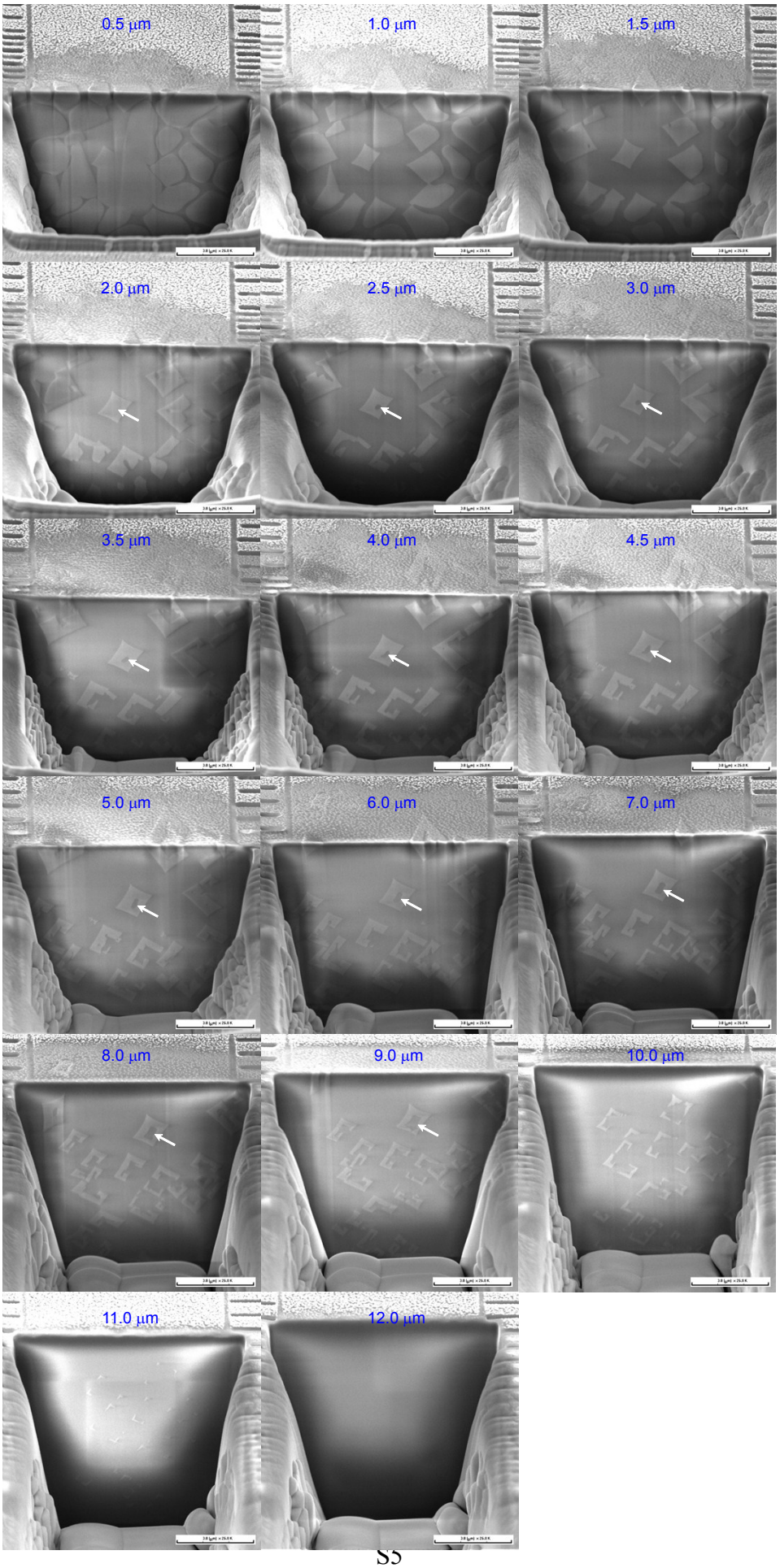
0.5 µm
1.0 µm
1.5 µm
2.0 µm
2.5 µm
3.0 µm
3.5 µm
4.0 µm
4.5 µm
5.0 µm
6.0 µm
7.0 µm
8.0 µm
9.0 µm
10.0 µm
11.0 µm
12.0 µm

Figure S4. 3D morphology evolution of the inter-diffusion-induced dendritic growth. γ-Al_2O_3 dendritic crystallites were first cut at a distance of 0.5 μm from the core/inter-crystalline-layer interface. The growth rate perpendicular to the *c*-axis main facets was lower than that of all other crystallographic direction, as predicted by the thermal kinetic model.[3] Then, it was milled in a step of 0.5 μm followed by 1 μm toward the glass cladding. After milling of 12.0 μm, the dendrites could no longer be observed. This clearly implies that the dendritic growth was not complete as the fiber was rapidly cooled to room temperature. Otherwise, the dendrite would have continued growing if the lower fiber drawing speeds were adopted. The positions from 9.0 to 2.5 μm, where the arrows highlight a compact γ-Al_2O_3 dendrite with an inclusion of residual glass, are particularly interesting and further show that the residual glass provided the supply for growth into an abnormally large size γ-Al_2O_3 (position 2.0 μm).

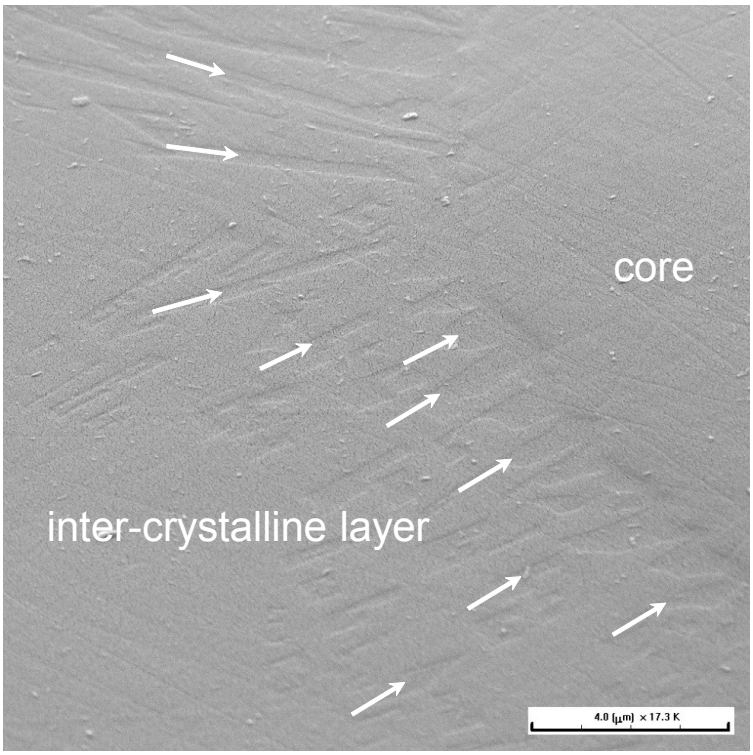

Figure S5. Interfacial morphology between the core and inter-crystalline layer. (a) Pristine SEM image of the interfacial structure. (b) Schematic of the interfacial structure from the perspective shown in (a), indicating that the faceted and lath-like dendrite grew into the inter-crystalline layer. Note that the rounding of the structural edges is an intentionally introduced artifact during mechanical preparations, showing distinctly different roughness signatures in the order of hardness: 1) sapphire core (27 GPa);[4] 2) γ-Al_2O_3 dendritic crystallite (2-6 GPa);[5] and 3) silica glass cladding (9 GPa).[6]

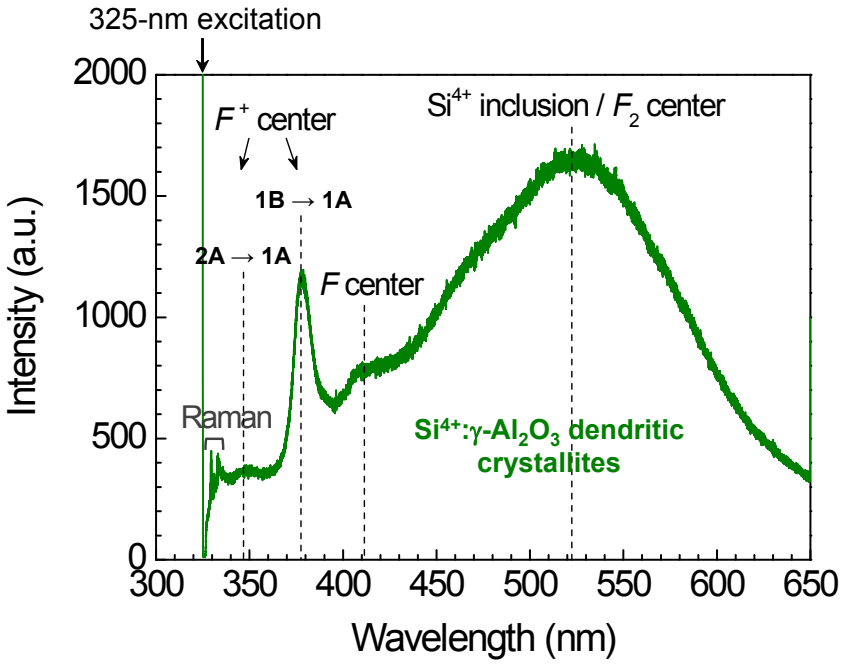

Figure S6. 325-nm-excited PL spectrum of the Si^{4+}:γ-Al_2O_3. Strong greenish broadband luminescence represents a considerable amount of oxygen vacancies and dopant emitters. These bands peaking at 347, 377, 412, and 523 nm are consistent with the known F^+ (an oxygen vacancy occupied by one electron)[7], F (an oxygen vacancy occupied by two electrons)[8] and Si^{4+}-related[9] (or F_2, an oxygen divancancy with four electrons[10]) color centers. Such ultraviolet-visible broadband emission is potentially beneficial to achieve ultra-high-resolution optical tomography for bioimaging owing to the spatial resolution being predominantly determined by the 3-dB bandwidth of the light source.[11]

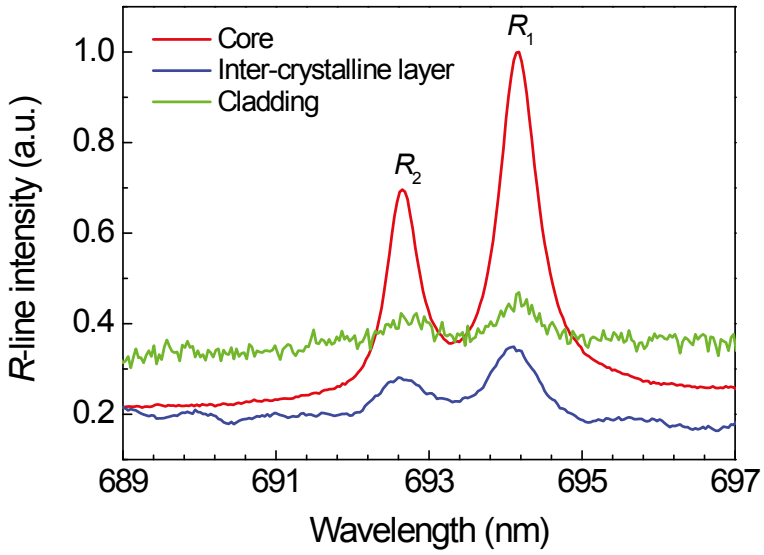

Figure S7. *R*-line spectra of the core, inter-crystalline layer and cladding. Zoom-in spectra of Figure 3b in the range of 689–697 nm, showing the two sharp *R* lines on the basis of the phonon side bands, attributable to the octahedral oxygen-coordinated Cr^{3+}.

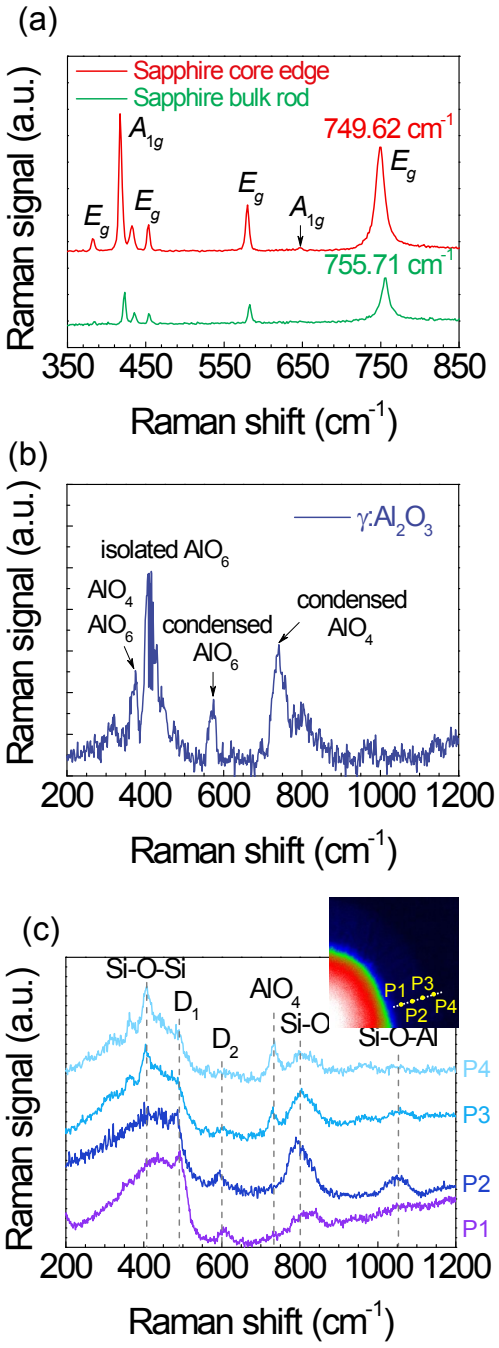

Figure S8. Representative Raman signatures. (a) the core, (b) γ-Al_2O_3 dendritic crystallite, and (c) cladding. A comparison between the core and bulk rod in (a) implies that the core edge suffered tensile stress relative to the starting material, as indicated by a blue-shifted E_g peak (cf. text below).

Fig. S8a shows the comparative full-range Raman spectra measured on the fiber core edge and on the starting bulk material, respectively. We detected seven prominent *c*-axis sapphire peaks, as labeled in Fig. S8a. It is noteworthy that the strongly enhanced Stokes signals of the hybrid fiber corroborate the effectiveness of the fiber waveguide confinement. Another salient

feature in Fig. S8a is that, compared to the starting sapphire rod, the fiber core edge shows a blue shift, indicating a strain-dependent Raman shift signature, as evident from the SAED *d*-spacings described in Section 3.2. The presence of this strain field within the LFD-fabricated hybrid fiber is mainly attributed to a TEC mismatch among the crystal core (4.5×10^{-6} °C^{-1}),[12] glass cladding (0.4×10^{-6} °C^{-1}),[13] γ-Al_2O_3 dendrite (8×10^{-6} °C^{-1}),[14] and inter-crystalline layer (7.6×10^{-6} °C^{-1}).[15] It should be noted that effective TEC of the inter-crystalline layer apparently can be reasonably estimated from alumino-silicate glass. This is because the inter-crystalline layer is a composite of γ-Al_2O_3 dendrites in the Al_2O_3–SiO_2 matrix on account of the inter-diffusion process. Although all the Raman modes are shifted toward a lower wavenumber, the E_g mode at 755 cm^{-1} presents a larger shift (749.62 cm^{-1} versus 755.71 cm^{-1}). Therefore, we chose this peak for the stress field analysis. It was shown that the 755-cm^{-1} E_g peak shift can be employed to estimate the residual internal stress in bulk sapphire.[16] Meanwhile, on the basis of the linear relation of the stress-induced Raman shift of 1.7 cm^{-1}/GPa in sapphire crystal,[16] we determined that the corresponding internal tensile stress change of 3.58 GPa accounted for the observed 6.09-cm^{-1} Raman shift, which is in agreement with the SAED *d*-spacing measurements (5.20 GPa).

Table S1 Experimentally and theoretically obtained *d* spacings in Si^{4+}:γ-Al_2O_3 dendritic crystallites

(*hkl*)	Experiment (nm)	Theory (nm)
(011)	0.5319	0.5586
(220)	0.2670	0.2800
(411)	0.1832	0.1862
(420)	0.1799	0.1766
(440)	0.131	0.1395

Fig. S8b shows the Raman spectrum of the γ-Al_2O_3 crystallites for the representative dendritic solidification in the inter-crystalline layer. Since there is a considerable polyhedral distortion in both tetrahedral and octahedral sites of the Si^{4+} and Cr^{3+} co-included γ-Al_2O_3 lattice, as indicated by the different *d*-spacings in Table S1, it is rationalized that the Raman peaks are blue-shifted from the wavenumbers 385 (bending AlO_4 and AlO_6), 420 (isolated AlO_6), 560 (condensed AlO_6), and 745 cm^{-1} (condensed AlO_4) reported for the pure undoped γ-Al_2O_3 prepared via a sol-gel route.[17] The distorted structure also reflects the appearance of Raman peaks being significantly broader than those of the undoped γ-Al_2O_3. Fig. S8c shows Raman spectra obtained from the glass matrix in the inter-crystalline layer, delineating clear features of vibrational modes of a typical alumino-silicate glass. The corresponding PL mapping is

shown in the inset of Fig. S8c, which depicts the positions for Raman studies. These four Raman spectra demonstrate the dependence on the radial distributions of γ- Al_2O_3 dendrites and silica contents, as addressed in the following discussion. The most prominent Raman mode peak at about 405 cm^{-1} is assigned to the Si-O-Si symmetric bending in the six-membered silicate rings;[18,19] whereas the two broader peaks emerging at ~490 and 600 cm^{-1} are due to the stretching mode of the defective three- and four-membered rings (denoted by D_2 and D_1) with a SiO_4 tetrahedra.[18–21] Additionally, the two peaks located at ~735 and 800 cm^{-1} are associated with Al-O bonds in the AlO_4 tetrahedral sites. The broad hump at 300–400 cm^{-1} is the convolution of the tetrahedral deformation vibrations of O-Si-O and O-Al-O bending.[22] In the high wavenumber range of 900–1200 cm^{-1}, several relatively feeble bands at around 960, 1050, and 1160 cm^{-1} belong to the bending vibrations of the Si-O-Al in the silica network. In Fig. S8c, it is observed that the predominant peak at 405 cm^{-1} is drastically reduced. This is accompanied by an increment of the D_1 and D_2 peaks as one toward the sapphire crystal core, which can be inferred as the densification of the glass network, that is, the onset of the nucleation of γ-Al_2O_3. This is further supported by the breaking of Si-O-Si bonding into defective three- and four-membered ring structures as a strong indication of Al_2O_3 incorporation into the SiO_2 matrix following the laser-induced inter-diffusion process, leading to an enhancement in the amount of SiO_4 tetrahedral sites with non-bridging oxygen. Meanwhile, the dramatically enhanced Raman bending modes in 900–1200 cm^{-1} is another important characteristic of the presence of high Al-rich content, which is pertinent to the present case of alumino-sodium silicate.[23]

REFERENCES

1. Y. S. Luh, R. S. Feigelson, M. M. Fejer and R. L. Byer, *J. Cryst. Growth*, 1986, **78**, 135.
2. A. E. Dixon, S. Damaskinos and M. R. Atkinson, *Nature*, 1991, **351**, 551.
3. P. F. Yan, K. Du and M. L. Sui, *Acta Mater.*, 2010, **58,** 3867.
4. W. G. Mao, Y. G. Shen and C. Lu, *J. Eur. Ceram. Soc.*, 2011, **31**, 1865.
5. M. R. Gallas, B. Hockey, A. Pechenik and G. J. Piermarini, *J. Am. Ceram. Soc.* 1994, **77**, 2107.
6. C. R. Kurkjian and G. W. Kammlott, *J. Am. Ceram. Soc.*, 1995, **78**, 737.
7. S. Liu, L. Zhang, Y. Fan, J. Luo, P. Zhang and L. An L. *Appl. Phys. Lett.*, 2006, **89**, 051911.
8. B. G. Draeger and G. P. Summers, *Phys. Rev. B*, 1979, **19**, 1172.
9. M. Baronskiy, A. Rastorguev, A. Zhuzhgov, A. Kostyukov, O. Krivoruchko and V. Snytnikov, *Opt. Mater.*, 2016, **53**, 87.
10. D. I. Tetelbaum, A. N. Mikhaylov, A. I. Belov, A. V. Ershov, E. A. Pitirimova, S. M. Plankina, V. N. Smirnov, A. I. Kovalev, R. Turan, S. Yerci, T. G. Finstad and S. Foss, *Phys. Solid State*, 2009, **51**, 385.

11. C. C. Lai, C. Y. Lo, T. H. Hsieh, W. S. Tsai, D. H. Nguyen and Y. R. Ma, *ACS Omega*, 2016, **1**, 552.
12. N. Ichinose, K. Shimamura, Y. Kaneko, E. A. G. Villora, K. Aoki, US Pat., 7629615, 2009.
13. Y. Kikuchi, H. Sudo and N. Kuzuu, *J. Appl. Phys*., 1997, **82**, 4121–4123.
14. W. R. Liu, Y. H. Li, W. F. Hsieh, C. H. Hsu, W. C. Lee, M. Hong and J. Kwo, *J. Phys. D: Appl. Phys.*, 2008, **41**, 065105.
15. G. Ghosh, *IEEE Photon. Technol. Lett.*, 1994, **6**, 431–433.
16. T. Wermelinger, C. Borgia, C. Solenthaler and R. Spolenak, *Acta Mater.*, 2007, **55**, 4657–4665.
17. P. V. Thomas, V. Ramakrishnan and V. K. Vaidyan, *Thin Solid Films*, 1989, **170**, 35–40.
18. M. Sakakura, M. Terazima, Y. Shimotsuma, K. Miura and K. Hirao, *J. Appl. Phys*., 2011, **109**, 023503.
19. M. Okuno, N. Zotov, M. Schmücker and H. Schneider, *J. Non-Cryst. Solids*, 2005, **351**, 1032–1038.
20. T. Seuthe, M. Grehn, A. Mermillod-Blondin, H. J. Eichler, J. Bonse and M. Eberstein, *Opt. Mater. Express*, 2013, **3**, 755–764.
21. W. L. Konijnendijk and M. Stevels, *J. Non-Cryst. Solids*, 1976, **20**, 193–224.
22. P. F. McMillan, A. Grzechnik and H. Chotalla, *J. Non-Cryst. Solids*, 1998, **226**, 239–248.
23. A. K. Yaday and P. A. Singh, *J. Non-Cryst. Solids*, 2015, **6**, 67583–67609.